Journal of
Synchrotron Radiation

ISSN 0909-0495

Received 25 June 2008
Accepted 8 October 2008

First XANES evidence of a disorder–order transition in a spinel ferrite compound: nanocrystalline $ZnFe_2O_4$

S. J. A. Figueroa[a,b] and S. J. Stewart[a]*

[a]IFLP-CCT-La Plata-CONICET and Departamento de Física, Facultad de Ciencias Exactas, CC 67, Universidad Nacional de La Plata, 1900 La Plata, Argentina, and [b]INIFTA, Facultad de Ciencias Exactas, UNLP and CCT-La Plata-CONICET, CC 16 sucursal 4, 1900 La Plata, Argentina.
E-mail: stewart@fisica.unlp.edu.ar

In situ Zn *K*-edge XANES experiments were performed to investigate the thermal evolution of the non-equilibrium state in nano-sized $ZnFe_2O_4$. The initially disordered ferrite was annealed under oxygen atmosphere and kept at temperatures of 673, 773 and 873 K. Modifications of the XANES features allowed the direct detection of the Zn local surrounding changes from O_h to T_d symmetry. Quantitative analyses of these results were performed by using the principal-component analysis approach. The ferrite inversion does not change until the activation barrier is overcome at T_a = 585 K. Above T_a, the Zn ions continuously change their environment to their normal equilibrium state. Isothermal treatments confirm that the Zn transference follows a first-order kinetic process. In addition, the thermal treatment produces a partial recrystallization that increases the average grain size from 13 to 50 nm and reduces the microstrain. The room-temperature magnetic state changes from ferrimagnetic to paramagnetic, while the blocking temperature increases after the treatment.

Keywords: XANES; Zn *K*-edge; PCA; zinc ferrite; $ZnFe_2O_4$.

1. Introduction

Amongst spinel ferrites MFe_2O_4 (where M is a 3d ion), zinc ferrite has become one of the most explored compounds during recent years (see, for example, Hochepied *et al.*, 2000; Chinnasamy *et al.*, 2002; Hoffman *et al.*, 2004; Stewart *et al.*, 2007). In its normal equilibrium state, Fe^{3+} and Zn^{2+} ions are surrounded by octahedral [B] and tetrahedral (A) oxygen arrays, respectively. The equilibrium distribution can be altered by employing non-equilibrium methods of synthesis (Hoffman *et al.*, 2004; Bohra *et al.*, 2006; Nakashima *et al.*, 2007*a*; Stewart *et al.*, 2007) or by reducing the $ZnFe_2O_4$ characteristic length down to nanometric ranges (Hochepied *et al.*, 2000; Atif *et al.*, 2006). This implies changes in its magnetic ordering that goes from antiferro to cluster-glass to ferrimagnetic state as the inversion, *i.e.* the fraction of (A) sites occupied by iron, increases (Hoffman *et al.*, 2004; Widatallah *et al.*, 2008).

Comprehension of the underlying mechanisms that favor a non-equilibrium cation distribution is relevant not only for fundamental studies but also for possible applications when a controllable magnetic response is required. In particular, as the magnetic degradation of ferrites might limit certain purposes (Lee *et al.*, 2006), it is also important to characterize the range of stability of the disordered ferrimagnetic state; in spite of the vast amount of published work on nanostructured $ZnFe_2O_4$, to our knowledge only a few studies have been performed to investigate its thermal stability (Šepelák *et al.*, 2004; Philip *et al.*, 2007). Šepelák *et al.* (2004) have studied the kinetics of disordered nanocrystalline high-energy milled $ZnFe_2O_4$. Through *in situ* X-ray diffraction (XRD) studies performed under air atmosphere, they found that the range of stability extends up to 600 K. Recently, Philip *et al.* (2007) also performed *in situ* XRD experiments on nano-sized $ZnFe_2O_4$. In this case the material, initially in its normal state, evolves towards a partially inverted state by heat treatment under vacuum. They also found that the cation redistribution starts at 1073 K. On the other hand, Pavese *et al.* (2000) had previously reported on the thermodynamic behavior of the thermally activated order–disorder transformation in bulk zinc ferrite. By using *in situ* neutron diffraction, they detected that an increment of the inversion parameter occurs above 800 K that smoothly increases up to 1500 K. These *in situ* investigations and others concerning the annealing effects on disordered $ZnFe_2O_4$ (Tung *et al.*, 2002; Nakashima *et al.*, 2007*b*) have provided significant information about the thermal stability of a particular distribution of cations. However, a comparison between these results may not be

straightforward as different initial material has been used and, in addition, different environmental conditions or rates of heating have been employed. Thus, more studies are needed to fully understand the mechanisms involved in the second-order transition that occurs in $ZnFe_2O_4$ that strongly affects its magnetism.

Recently, X-ray absorption near-edge structure (XANES) experimental and *ab initio* simulation results on disordered $ZnFe_2O_4$ provided direct evidence of Zn^{2+} and Fe^{3+} transferences from equilibrium to non-equilibrium sites as the inversion increases (Stewart *et al.*, 2007). Analogous effects were observed by Nakashima *et al.* (2007*a*) in their Fe and Zn *K*-edge XANES spectra of disordered $ZnFe_2O_4$ thin films, which were also reproduced by simulations using a first-principles method. These independent investigations provided a semi-quantitative determination of the inversion in $ZnFe_2O_4$, in good agreement with the inversion obtained by the extended X-ray absorption fine-structure (EXAFS) fitting analysis. These findings allowed a not always clear identification of XANES features as a function of the local structure of the compound, opening a new perspective to explore XANES as a tool to investigate the disorder $\leftrightarrow$ order transition in spinel ferrites. For instance, XANES spectroscopy under dispersive geometry involves a shorter time for data collection when compared with EXAFS or diffraction techniques, which makes it appropriate for kinetics studies. It also represents an alternative to the diffraction *in situ* experiments performed on nanocrystalline $ZnFe_2O_4$, whose results are characterized by broad reflection lines that, added to thermal effects, might make it difficult to obtain reliable structural and inversion parameters during a treatment.

We present here an investigation of the thermal stability of partially inverted nano-sized $ZnFe_2O_4$ by employing, for the first time, *in situ* time-resolved XANES experiments. We will demonstrate that the thermal evolution of Zn *K*-edge XANES spectra allows us to follow the thermally activated relocation of zinc ions towards their equilibrium positions. This study is complemented by performing *ex situ* X-ray diffraction, XANES, EXAFS and magnetic measurements.

2. Experiment

Partially inverted $ZnFe_2O_4$ nanoferrite (degree of inversion determined by EXAFS analysis, $c = 0.4$, average grain size $D =$ 13 nm) was obtained by milling hydrothermally prepared nanocrystalline $ZnFe_2O_4$ ($c = 0.2$, $D = 6$ nm). Details of sample preparation can be found elsewhere (Stewart *et al.*, 2007). *In situ* XANES spectra at the Zn *K*-edge (9659 eV) were collected in transmission mode using the D06A-DXAS beamline at LNLS (Laboratório Nacional de Luz Síncrotron) in Campinas, Brazil. A curved crystal monochromator selects a bandwidth of hundreds of eV around absorption edges, according to the Bragg angle and radius of curvature. Details of the experimental set-up of the beamline have been published elsewhere (Tolentino *et al.*, 2005). The XANES experiments were performed in a controlled-atmosphere cell (Meneses *et al.*, 2006), heating the inverted zinc ferrite sample at a rate of 10 K min^{-1} in an oxygen flow from ambient temperature up to 673 K for 60 min (step *X*), 773 K for 60 min (step *Y*) and 873 K for 120 min (step *Z*). Afterwards the furnace was switched off and the sample was allowed to cool down inside the cell under oxygen flow. The data analysis was performed by subtracting a linear background and rescaling the absorbance by normalizing the difference between the baseline and the post-edge absorption in a region approximately 300 eV behind the edge. A Fortran program was used (Fernández-García *et al.*, 1995) to analyze the XANES data using principal-component factor analysis.

XANES and EXAFS *ex situ* spectra (Zn and Fe *K*-edges) of the sample before and after the treatment were collected at room temperature in transmission mode using a Si(111) monochromator with a slit aperture of 0.3 mm at the XAFS-1 beamline of the LNLS. The $\chi(k)$ EXAFS signal was extracted using the *Athena* program and analyzed using the *Arthemis* program (Ravel & Newville, 2005).

XRD patterns at room temperature were taken using a Philips PW 1710 diffractometer (Cu $K\alpha$ radiation with $\lambda =$ 1.5406 Å). XRD data were collected at room temperature in the $20^\circ \leq 2\theta \leq 120^\circ$ range, with 0.02° step width and counting rate of 10 s per step. Magnetic measurements were carried out using a SQUID magnetometer (Quantum Design) and an AC susceptometer (Lakeshore).

3. Results and discussion

3.1. X-ray absorption results

X-ray absorption near-edge spectra at the Zn *K*-edge are a sign of the electronic transition from the zinc 1*s* core level to unoccupied *p*-type states. Zn *K*-edge XANES of normal spinel $ZnFe_2O_4$ consists of three resolved peaks, *A*, *B* and *C* (Fig. 1), at around 9664, 9668 and 9672 eV, respectively, a shoulder at around 9677 eV (peak *D*), plus additional structure at higher

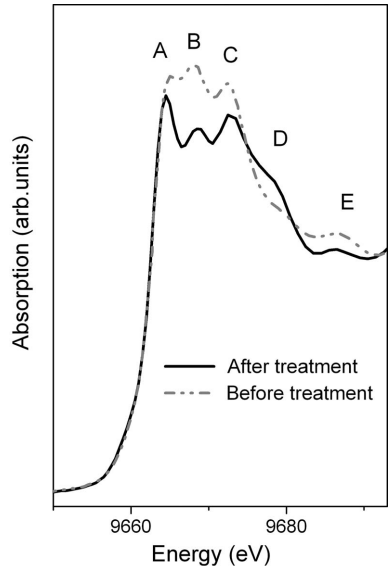

Figure 1
Ex situ Zn *K*-edge XANES spectra taken at room temperature of nano-sized $ZnFe_2O_4$ before and after the thermal treatment.

energies (peak *E*) (Waychunas *et al.*, 2003; Stewart *et al.*, 2007). These features were adequately reproduced by means of *ab initio* calculations using the *FEFF8.2* code (Ankudinov *et al.*, 1998) considering the electron scattering from the ligand shell surrounding the Zn absorber (Stewart *et al.*, 2007).

Experimentally, we found that as $ZnFe_2O_4$ becomes partially inverted the intensity of the second peak *B* [labelled *A*1 in Stewart *et al.* (2007)] progressively increases and the shoulder *D* weakens (line *A*2). These trends were also confirmed by our calculation results. Indeed, the theoretical spectra generated by assuming a weighted sum of the spectrum with Zn at its equilibrium tetrahedral sites plus the spectrum corresponding to Zn substitutional to the Fe atoms at octahedral sites are in very good agreement with our experimental findings (Stewart *et al.*, 2007). In particular, the *B* peak is a signature of the white line corresponding to Zn substitutional to Fe in the spinel structure, whose theoretical spectrum is also characterized by the almost absence of peak *D* (Waychunas *et al.*, 2003; Stewart *et al.*, 2007). These effects of inversion on the Zn *K*-edge XANES were later corroborated by Nakashima *et al.* (2007) in their study about $ZnFe_2O_4$ thin films with a disordered cation distribution. Moreover, they reproduced the features of the $ZnFe_2O_4$ XANES spectra at Zn and Fe *K*-edges throughout simulations using first-principles calculations based on density functional theory. Their results also showed that the middle peak contribution increases when Zn^{2+} at octahedral sites is considered while the peak at *D* corresponds to an electronic transition that involves Zn sites with T_d symmetry.

To investigate the thermal stability of partially inverted $ZnFe_2O_4$ we have performed *in situ* XANES experiments at the Zn *K*-edge. Owing to its initial inversion ($c = 0.4$), XANES spectra taken before the treatment show the enhancement of peak *B* and the almost absence of the shoulder *D* when compared with the spectrum of normal $ZnFe_2O_4$ (Stewart *et al.*, 2007).

We observe that, as nanocrystalline disordered $ZnFe_2O_4$ is annealed, a progressive recovering of the normal spinel XANES features takes place, *i.e.* the middle peak *B* decreases and the shoulder *D* becomes more noticeable after annealing. This tendency can be visualized through color contour curves of the absorption spectra, as shown in Fig. 2. Indeed, we distinguish an initial state with a white line centralized at about 9668 eV, while the final state clearly shows the four features *A*, *B*, *C* and *D* that characterize XANES of normal $ZnFe_2O_4$ (see also Fig. 1). This trend is reversed to the behavior observed as the inversion increases (Stewart *et al.*, 2007). Therefore, considering the previous results, we assign this change as an indication that the Zn local environment is changing from O_h to T_d symmetry with the treatment.

To further characterize the thermally activated disorder–order transition we performed a principal-component analysis (PCA). PCA consists of a statistical methodology applied on a set of normalized energy calibrated spectra (Malinowski & Howery, 1980), which has become an important tool for the recognition of components using XANES data provided the presence of clearly dissimilar features of each individual species. Thus, taking into account the different features that distinguish Zn *K*-edge XANES of partially inverted from normal $ZnFe_2O_4$, we generated the spectra as a linear combination of these two components to roughly estimate the proportion of each site by using this approach. Table 1 shows the calculated eigenvalues with their respective variance, the percentage significance level (%SL) and the IND, an empirical function used to help in deciding the number of components (Malinowski & Howery, 1980). Assuming a 5% test level for %SL, the PCA would indicate the presence of two principal components in the thermal treatment. However, the IND function suggests that a seventh principal component could be present (Table 1). However, the lack of importance of this possible component can be tested visually by examining the abstract row matrix in Fig. 3. Indeed, it can be seen that the first two factors (1 and 2) represent most of the signal while the third and subsequent are mainly dominated by noise and low-frequency background components. On the other hand, Table 1 points out the very low contributions to the variance made by eigenvalues higher than the second one. Consequently, the number of principal components has been fixed at two. Fig. 4 shows the result of PCA by considering some selected spectra. The result of this analysis shows that the

Table 1
Eigenvalues from the PCA, their variance, the percentage significance level (%SL) and the IND, the empirical function used to determine the number of components (*n*).

n	Eigenvalue	Variance†	%SL	IND × 10^{-4}
1	1697.7	99.966	0.0	0.740
2	0.53851	0.032	0.0	0.217
3	0.013794	0.001	6.06	0.202
4	0.0091835		5.51	0.185
5	0.0057103		5.24	0.168
6	0.0030411		7.10	0.158
7	0.0009242		25.78	0.175
8	0.0007361		27.32	0.199
9	0.00054870		30.84	0.234
10	0.00033881		40.32	0.294

† Variances lower than 10^{-3} are not reported.

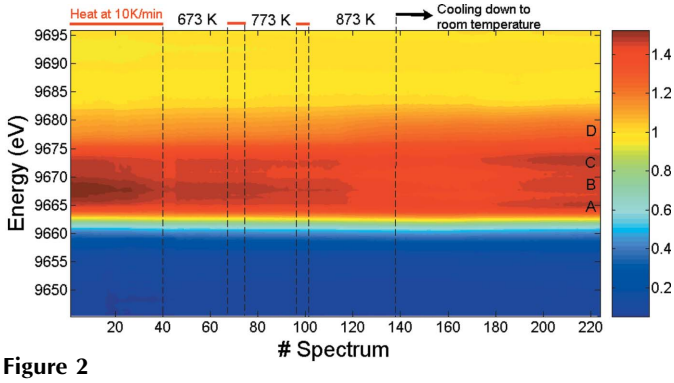

Figure 2
Color contour map of the absorption spectra recorded under *in situ* conditions. The annealing temperatures at steps *X*, *Y* and *Z* are indicated at the top. The heating rate was kept to 10 K min^{-1}. The blue region indicates the pre-edge contribution while the dark red region represents the position of the white line. The discontinuity of the white line between spectra 40 and 47 is due to intensity saturation.

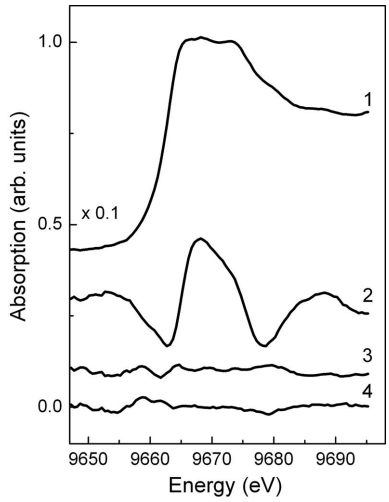

Figure 3
Abstract component matrix for the selected spectra at the Zn *K*-edge.

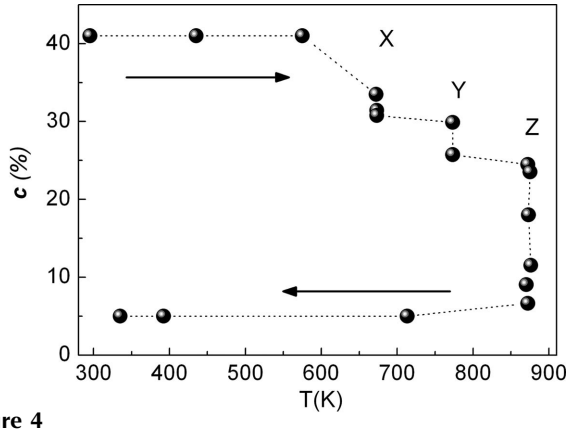

Figure 4
Thermal dependence of the inversion *c* obtained by performing a PCA of the data.

inversion does not change on heating until the activation barrier is overcome at about $T_a = 585$ K (Figs. 2 and 4). Above T_a the Zn ions continuously change their local environment to an equilibrium state along the maximum temperature studied (step *Z*, $T_{max} = 873$ K) and continue along the equilibrium pathway on cooling.

After the activation barrier is surmounted, the inversion during heating (10 K min^{-1}) decreases following a linear behavior with time, $c/c_i = 1 - \alpha t$, where $\alpha = 1.4 \times 10^{-3}$ s^{-1} and c_i is the initial inversion. A relaxation process towards equilibrium is also observed at each isotherm. Fig. 5 shows the time dependency of the relative degree of inversion c/c_0 when the ferrite sample remains at the isotherm $T = 873$ K (c_0 is the initial inversion at the beginning of step *Z*). Following the assumption made by Šepelák *et al.* (2004) to analyze their *in situ* XRD data, we supposed a relaxation towards a normal spinel configuration controlled by a kinetic process obeying an exponential law. Fitting c/c_0 *versus* time data by using the function $c/c_0 = \exp[k(t - t_0)]$ gives a rate constant $k \simeq 0.01$ min^{-1} and an induction time $t_0 \simeq 20$ min.

Fourier transforms (FTs) of the $k^3\chi(k)$ EXAFS signal at Zn and Fe *K*-edges without phase correction for the sample after

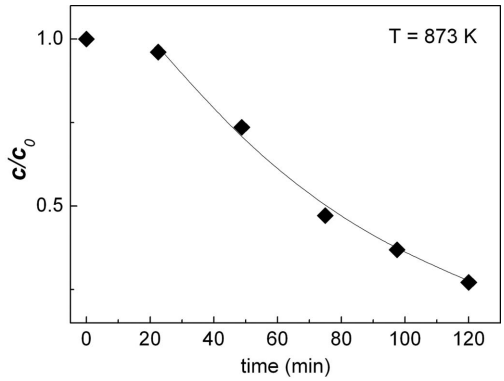

Figure 5
Isothermal kinetics of the Zn transference in nano-sized $ZnFe_2O_4$ at $T = 873$ K (step *Z*). The solid line corresponds to the fitting considering an exponential law.

the thermal treatment are shown in Fig. 6, while fit results are summarized in Table 2. From the FTs of the Zn *K*-edge spectra we observe an almost disappearance of the peak corresponding to Zn octahedrally coordinated at $R \simeq 2.95$ Å, which was clearly visible in the FTs corresponding to the sample before the treatment (Stewart *et al.*, 2007). Furthermore, these FTs resemble those of bulk $ZnFe_2O_4$ (Stewart *et al.*, 2007). This is in accordance with the thermally activated $Zn[B] \rightarrow Zn(A)$ transference illustrated by the present XANES studies. From these EXAFS data we found that after completing the treatment the inversion parameter $c \simeq 0.05$, *i.e.* almost the same inversion that we estimated for bulk $ZnFe_2O_4$.

3.2. Thermally induced structural and magnetic changes in $ZnFe_2O_4$ nanoparticles

The XRD pattern of the thermally treated zinc ferrite only showed the peaks belonging to $ZnFe_2O_4$ (see inset of Fig. 7) with narrowed linewidths when compared with those before the treatment (Fig. 7). Considering the corrected integral breadth, β, of the most intense reflection (311), we estimated, by means of Scherrer's equation, the average grain size (D). Also, from the relation $\beta = 4(\Delta d/d)\tan\theta$ we found the average microstrain level, $\varepsilon = \Delta d/d$. The results show that D has grown to 50 nm and ε has decreased by 40%. Furthermore, the cell parameter changes from $a = 8.435$ to 8.439 Å. This lattice dilation might be associated with the evolution towards a less disordered state owing to more Zn^{2+} with higher radius than Fe^{3+} occupying *A* sites after the calcinations ($a = 8.441$ Å for normal bulk $ZnFe_2O_4$).

Fig. 8 shows magnetization *versus* applied magnetic field (*M*–*H*) before and after the treatment. *M*–*H* of initial inverted ferrite shows a sigmoidal shape with a high magnetization owing to its ferrimagnetic state. This state comes from the occupancy of Fe^{3+} at both *B* and *A* sites that promotes the action of J_{AB} superexchange interactions that give rise to the ferrimagnetic ordering. After the treatment, the ferrimagnetic state at room temperature is almost eradicated (Fig. 8), as can be observed by the almost disappearance of the sigmoidal shape and the linear increment of *M* for all values of the field. This indicates that, in addition to the Zn^{2+} redistribution as

Table 2
EXAFS Fe and Zn *K*-edge fitted parameters for $ZnFe_2O_4$ after thermal treatment.

N is the coordination number, *R* is the distance from the central atom, σ^2 is the Debye–Waller factor and E_0 is the energy shift.

Edge	Shell	*N*	*R* (Å)	$\sigma^2 \times 10^{-2}$ (Å^2)	E_0 (eV)
K-Fe	O	5.9 ± 0.6	2.01 ± 0.01	0.6 ± 0.1	−7.4 ± 0.6
	Fe	5.9 ± 0.6	2.989 ± 0.004	0.6 ± 0.06	−7.4 ± 0.6
	O	2 ± 0.2	3.49 ± 0.01	0.95 ± 0.09	−7.4 ± 0.6
	Zn	5.9 ± 0.6	3.51 ± 0.01	0.95 ± 0.09	−7.4 ± 0.6
K-Zn	O	3.8 ± 0.4	2.003 ± 0.007	0.4 ± 0.3	4 ± 1
	Fe	11 ± 1	3.54 ± 0.04	1.0 ± 0.2	4 ± 1
	O	11 ± 1	3.57 ± 0.04	1.0 ± 0.2	4 ± 1
	Zn	3.7 ± 0.3	3.69 ± 0.04	1.0 ± 0.2	4 ± 1

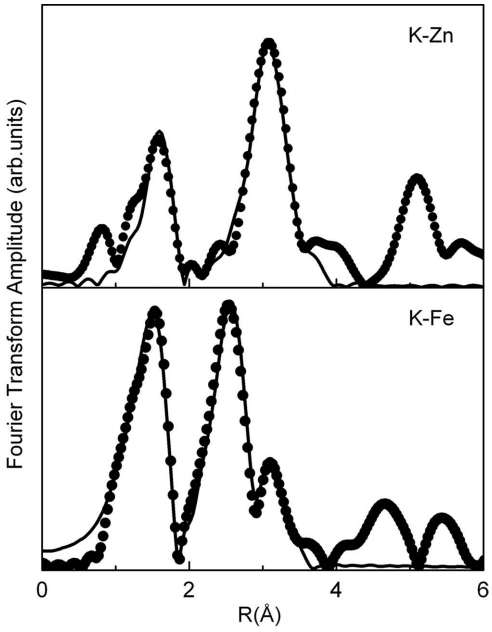

Figure 6
Fourier transforms of $k^3\chi(k)$ EXAFS data at the Zn and Fe *K*-edges taken *ex situ* for nanocrystalline $ZnFe_2O_4$ after completing the thermal treatment following the steps *X*, *Y* and *Z*. The solid lines are the fitting results corresponding to the parameters shown in Table 2.

observed by the Zn *K*-edge XANES, Fe^{3+} ions are also changing their local environment from T_d to O_h symmetry or are being transferred to occupy their equilibrium position.

Fig. 9 shows the in-phase component of the AC susceptibility, χ. We observe that, after the annealing, the χ maximum has shifted towards lower temperatures by about 170 K. The temperature at which the maximum occurs is associated with the blocking temperature, T_B, of the particle moments. Considering the Brown–Néel model, the anisotropy energy E_a for independent moments is related to T_B as $E_a = k_B T_B \ln(\tau/\tau_0)$, where τ_0 is a factor in the range 10^{-9}–10^{-12} s, and k_B is Boltzmann's constant. When assuming a uniaxial anisotropy, $E_a = K_{eff}V$, where K_{eff} is the anisotropy constant and V is the volume of the magnetic particles. Therefore, the decrease of T_B can be associated with a reduction of the apparent magnetic size or a decrease of K_{eff} owing to a reduction of the surface anisotropy (Tung *et al.*, 2002). Indeed, thermal activated relocations of type $Zn^{2+}[B] \rightarrow Zn^{2+}(A)$ and

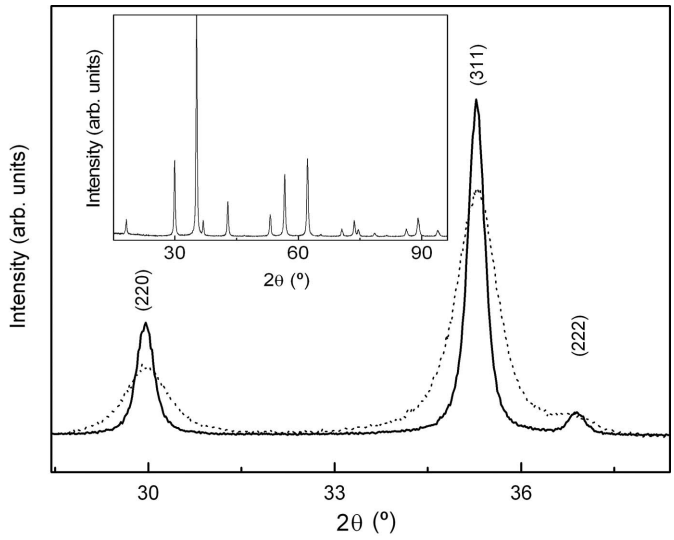

Figure 7
A region of the X-ray diffraction patterns of $ZnFe_2O_4$ before and after treatment and of bulk $ZnFe_2O_4$. Inset: whole X-ray diffraction pattern of $ZnFe_2O_4$ after completing treatment through steps *X*, *Y* and *Z*.

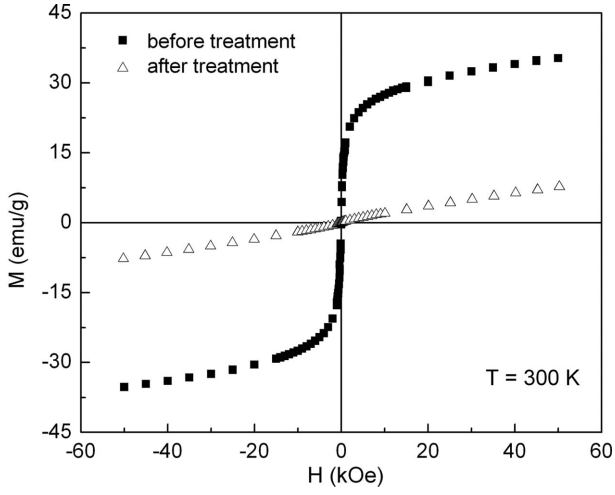

Figure 8
Magnetization *versus* applied magnetic field curves taken at room temperature for $ZnFe_2O_4$ before and after treatment.

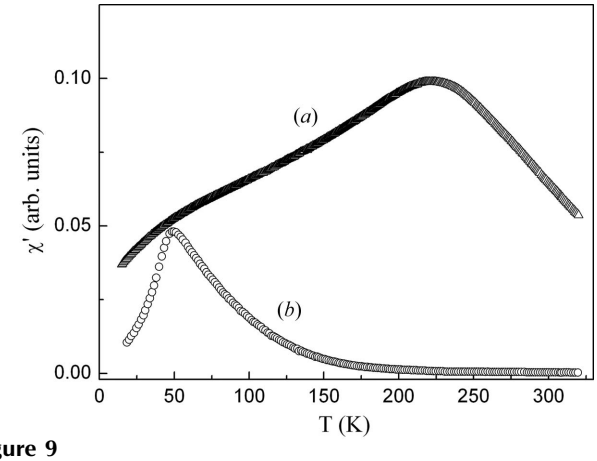

Figure 9
Thermal dependence of the low-field in-phase component of the AC-susceptibility (χ) of $ZnFe_2O_4$ before (*a*) and after (*b*) treatment.

$Fe^{3+}(A) \rightarrow Fe^{3+}[B]$ suggest that pathways Fe[*B*]—O— Fe(*A*) become less probable. This would also imply a reduction in the magnetic cluster sizes and the consequent decrease in T_B.

3.3. Comments about the disorder–order transition in nano-sized $ZnFe_2O_4$

Our results relating to the thermal stability of the disordered state in nano-sized $ZnFe_2O_4$ show a good agreement with those reported by Šepelák *et al.* (2004). We can infer that, independent of whether the annealing is performed under air or oxygen flow, the stability of the non-equilibrium cation extends up to 585–600 K. Thus, probably owing to its metastable character, the disorder → order transition activates at a lower temperature than the order → disorder transition (Pavese *et al.*, 2000; Philip *et al.*, 2007). However, some questions remain unanswered regarding the mechanism involved in these transitions. Usually they are depicted as a movement or redistribution of cations between the spinel interstitial sites. However, it is uncertain whether there is a hopping of cations or the transition involves a rearrangement of oxygen atoms that mainly affects the surface layer. It seems that to generate the order → disorder change the creation of oxygen vacancies is necessary (Pavese *et al.*, 2000; Philip *et al.*, 2007). On the other hand, milling $ZnFe_2O_4$ always causes an inversion enhancement, independent of whether the particle/grain sizes decrease (Hoffman *et al.*, 2004) or increase (Stewart *et al.*, 2007). This would imply that milling not only affects the surface but involves the whole particle, causing an accumulation of defects that favors a non-equilibrium distribution of cations. When the thermal treatment is performed in such a way that the material has oxygen available, it stabilizes in its normal state (Šepelák *et al.*, 2004; Philip *et al.*, 2007). Thus, all these results would point out that the oxygen mobility is playing an important role, but more investigations are required to interpret the configuration changes in spinel compounds that strongly influence their physical properties.

4. Conclusions

By means of Zn *K*-edge *in situ* XANES experiments we were able to directly observe the zinc transference from non-equilibrium octahedral positions to equilibrium tetrahedral ones within the spinel structure of ferrimagnetic $ZnFe_2O_4$ nanoparticles. We found that the activation of the disorder–order transition takes place above 585 K and intensifies with temperature. Isothermal treatments showed that the Zn transference follows a first-order kinetic process. Additional results indicate that the thermal treatment produces a partial recrystallization that increases the average grain size from 13 to 50 nm and reduces the microstrain. Once the activation barrier is overcome, the cation configuration (Fe and Zn) moves towards equilibrium and consequently the spontaneous magnetization of the initial ferrimagnetic state starts to be erased. Finally, these results demonstrate the feasibility of XANES spectroscopy to gain insight into the order ↔ disorder transitions in Zn-containing spinel compounds.

SJAF is a Fellow of CONICET, Argentina; SJS is a member of Carrera del Investigador Científico, CONICET, whose financial support is acknowledged. We appreciate financial support from LNLS, Campinas, SP, Brazil (proposals D06A-DXAS-4812 and D04B-XAFS1-4148), CONICET (PIP 6524, PIP 6075) and ANPCyT, Argentina (PICT 38337). We thank S. G. Marchetti and J. F. Bengoa for sample preparation, and F. García and G. Azevedo for kind assistance during the X-ray absorption experiments.

References

Ankudinov, A. L., Ravel, B., Rehr, J. J. & Conradson, S. D. (1998). *Phys. Rev. B*, **58**, 7565–7576.
Atif, M., Hasanain, S. K. & Nadeem, M. (2006). *Solid State Commun.* **138**, 416–421.
Bohra, M., Prasad, S., Kumar, N., Misra, D. S., Sahoo, S. C., Venkataramani, N. & Krishnan, R. (2006). *Appl. Phys. Lett.* **88**, 262506.
Chinnasamy, C. N., Narayanasamy, A., Ponpandian, N., Justin Joseyphus, R., Jeyadevan, B., Tohji, K. & Chattopadhyay, K. (2002). *J. Magn. Magn. Mater.* **238**, 281–287.
Fernández-García, M., Marquéz, C. & Haller, G. L. (1995). *J. Phys. Chem.* **99**, 12565–12569.
Hochepied, J. F., Bonville, P. & Pileni, M. P. (2000). *J. Phys. Chem. B*, **104**, 905–912.
Hoffman, M., Campbell, S. J., Ehrardt, H. & Feyerherm, R. (2004). *J. Mater. Sci. Lett.* **39**, 5057–5065.
Lee, S. W., Bae, S., Takemura, Y., Yamashita, E., Kunisaki, J., Zurn, S. & Kim, C. S. (2006). *IEEE Trans. Magn.* **42**, 2833–2835.
Malinowski, E. R. & Howery, D. G. (1980). *Factor Analysis in Chemistry.* New York: Wiley.
Meneses, C. T., Flores, W. H., Sotero, A. P., Tamura, E., Garcia, F. & Sasaki, J. M. (2006). *J. Synchrotron Rad.* **13**, 468–470.
Nakashima, S., Fujita, K., Tanaka, K., Hirao, K., Yamamoto, T. & Tanaka, I. (2007*a*). *Phys. Rev. B*, **75**, 174443.
Nakashima, S., Fujita, K., Tanaka, K., Hirao, K., Yamamoto, T. & Tanaka, I. (2007*b*). *J. Magn. Magn. Mater.* **310**, 2543–2545.
Pavese, A., Levy, D. & Hoser, A. (2000). *Am. Mineral.* **85**, 1497–1502.
Philip, J., Gnanaprakash, G., Panneerselvam, G., Antony, M. P., Jayakumar, T. & Raj, B. (2007). *J. Appl. Phys.* **102**, 054305.
Ravel, B. & Newville, M. (2005). *J. Synchrotron Rad.* **12**, 537–541.
Šepelák, V., Wilde, L., Steinike, U. & Becker, K. D. (2004). *Mater. Sci. Eng. A*, **375–377**, 865–868.
Stewart, S. J., Figueroa, S. J. A., Ramallo López, J. M., Marchetti, S. G., Bengoa, J. F., Prado, R. J. & Requejo, F. G. (2007). *Phys. Rev. B*, **75**, 073408 (arxiv:cond-Mater/0611532).
Tolentino, H. C. N., Cezar, J. C., Watanabe, N., Piamonteze, C., Souza Neto, N. M., Tamura, E., Ramos, A. Y. & Neuenschwander, R. T. (2005). *Phys. Scr.* T**115**, 977–979.
Tung, L. D., Kolesnichenko, V., Caruntu, G., Caruntu, D., Remond, Y., Golub, V. O., O'Connor, C. J. & Spinu, L. (2002). *Physica B*, **319**, 116–121.
Waychunas, G. A., Fuller, C. C., Davis, J. A. & Rehr, J. J. (2003). *Geochim. Cosmochim. Acta*, **67**, 1031–1043.
Widatallah, H. M., Al-Omari, I. A., Sives, F., Sturla, M. B. & Stewart, S. J. (2008). *J. Magn. Magn. Mater.* **320**, e324–e326.